

# Enhancing internal electric field of 3D porous chitosan-PDI polymer with donor-acceptor structure for efficient photocatalytic advanced oxidation



Sijie Huang <sup>a,1</sup>, Hanjie Zhang <sup>b,1</sup>, Wenting Li <sup>a,\*</sup>, Liping Liu <sup>a</sup>, Jingyi Xu <sup>a</sup>, Meichi Chong <sup>a</sup>, Junshan Li <sup>c</sup>, Yongfa Zhu <sup>a,\*</sup>

<sup>a</sup> Department of Chemistry, Tsinghua University, Beijing 100084, China

<sup>b</sup> Beijing Key Laboratory of Research and Application for Aerospace Green Propellants, Beijing Institute of Aerospace Testing Technology, Beijing 100074, China

<sup>c</sup> Institute for Advanced Study, Chengdu University, Chengdu 610106, China

## ARTICLE INFO

### Keywords:

Photocatalysis  
Internal electric field  
Charge separation  
PDS activation

## ABSTRACT

The charge separation efficiency of photocatalysts remains a formidable challenge for visible light-driven advanced oxidation. Herein, a three-dimensional (3D) porous PDI-CTS photocatalyst with donor-acceptor (D-A) structure was synthesized and showed an impressive bisphenol A (BPA) degradation rate of  $0.343 \text{ min}^{-1}$  through peroxydisulfate (PDS) activation. The D-A interaction facilitates charge transfer from CTS to PDI, inducing a larger molecular dipole moment than pure PDCTA. Thus, robust internal electric field with 6.9 times enhancement was built up in PDI-CTS, facilitating the separation of photogenerated carriers. Moreover, multiple PDI active sites provided by 3D porous PDI-CTS were conducive to the adsorption of pollutants, and generated more electron-enriched PDI<sup>+</sup> for PDS activation. Since PDS captures electrons from PDI<sup>+</sup>, the migration of holes to the surface is further improved, resulting in a remarkable mineralization rate of 87%. This work develops a unique D-A photocatalyst to promote photogenerated carriers migration for efficient photocatalytic advanced oxidation.

## 1. Introduction

As an economical and convenient wastewater purification technology, photocatalytic activated advanced oxidation process (APOs) has been widely concerned [1–3]. One of the critical steps involves the activation of peroxydisulfate (PDS) [4,5] through the photogenerated electrons ( $e^-$ ) produced by the photocatalyst, thus generating strongly oxidized sulfate radicals ( $\text{SO}_4^{\cdot-}$ ) [6,7] and hydroxyl radicals ( $\cdot\text{OH}$ ) [8] to oxidize and mineralize pollutants. However, insufficient active sites and severe recombination of photogenerated carriers in photocatalyst limit the effective activation of PDS [9], preventing photocatalytic APOs. Therefore, it is necessary to design photocatalyst with high charge separation and multi-active sites to achieve efficient degradation and deep mineralization.

To increase charge separation efficiency and enhance the surface reaction rate, it can be achieved by constructing heterojunction [10–13], increasing crystallinity [14–16] and constructing three-dimensional (3D) structure [17–20]. Among them, the construction of 3D structure

has more prominent advantages. For example, the unique porous structure can effectively enhance the adsorption and enrichment capacity of pollutants and promote surface reaction [21]. At the same time, increasing the exposure of reactive sites is conducive to the formation of more photogenerated carriers involved in the reaction [22]. Moreover, the rich and open multi-channel structure allows the light source to be reflected multiple times, thus improving the light absorption capacity [23]. It is noteworthy that the 3D network structure can effectively prevent material agglomeration and improve structural stability and reusability [24].

Internal electric field (IEF) engineering has emerged as an efficient method to promote photogenerated charge separation in photocatalysts [25–32]. Organic photocatalysts with large delocalization system and high spectral efficiency can modify their molecular dipoles by grafting suitable substituents to promote IEF, which has a positive effect on the separation of photogenerated charge [33,34]. Therefore, we proposed that the construction of 3D porous photocatalysts with electron donor-acceptor (D-A) characteristics can increase molecular dipoles,

\* Corresponding authors.

E-mail addresses: [lmt21@mails.tsinghua.edu.cn](mailto:lmt21@mails.tsinghua.edu.cn) (W. Li), [zhuyf@tsinghua.edu.cn](mailto:zhuyf@tsinghua.edu.cn) (Y. Zhu).

<sup>1</sup> These authors contributed equally

thereby enhancing IEF and increasing the driving force of photo-generated carrier separation.

Herein, 3,4,9,10-perylene tetracarboxylic dianhydride (PTCDA) and chitosan (CTS) were covalently linked and freeze-dried to obtain perylene diimide-chitosan (PDI-CTS). The 3D porous PDI-CTS has the large specific surface area and pore volume, which is expected to enhance the adsorption and enrichment of pollutants and PDS, thus accelerating the surface reaction process. Based on the donor-acceptor (D-A) interaction, electrons transfer from CTS to PDI induces an enlarged dipole of PDI-CTS, establishing a strong internal electric field to enhance photo-generated carrier separation. Under visible light irradiation, the D-A interaction promotes electron transfer of PDI-CTS, forming more electron-enriched PDI<sup>·</sup>. Subsequently, the electrons of PDI<sup>·</sup> can be captured by PDS, leading to rapid activation of PDS. This process is also expected to facilitate the efficient degradation through the synergistic effect of various reactive species, such as SO<sub>4</sub><sup>2-</sup>, ·OH, ·O<sub>2</sub> and h<sup>+</sup>. Notably, the photocatalytic-assisted PDS activation further promotes the migration of strongly oxidized h<sup>+</sup>, resulting in the deep mineralization of organic pollutions. The PDI-CTS photocatalyst with high charge separation efficiency and multiple active sites provided a unique perspective for efficient PDS activation and deep mineralization of pollutants.

## 2. Experimental section

### 2.1. Synthetic procedures of PDI-CTS

2.00 g PTCDA, 1.64 g CTS and 20.00 g imidazole were stirred for 48 h at 140 °C. Add 200 mL anhydrous ethanol and 100 mL HCl, and stirred for 1 day. The suspension was filtered with 0.45 µm membrane, and then washed with 600 mL aqueous solution containing 60 g KOH and 48 g KCl for several times to remove the unreacted PTCDA. Afterwards, the precipitate was transferred to 200 mL 10% hydrochloric acid and stirred for 24 h to neutralize the remaining alkali. The brown product PDI-CTS was obtained from the precipitation by filtration, water washing and freeze-drying [Scheme 1](#).

### 2.2. Preparation of PDINH, PTCDA and PDIPA

Perylene diimide (PDINH) was prepared according to the previous reported [\[35\]](#). 1.00 g PDINH was dispersed in 100 mL H<sub>2</sub>SO<sub>4</sub> ultrasound for 10 min and then poured into 1 L deionized water. Afterwards, it was filtered and washed to neutralize, and dried at 60 °C to obtain PDINH. According to the same method, self-assembled PTCDA was prepared.

Perylene diimide propionic acid (PDIPA) was prepared based on previous reported [\[36\]](#). (a) 1.37 g PTCDA, 18.00 g imidazole, 2.49 g 3-aminopropionic acid (PA) were stirred at 100 °C for 4 h. Afterwards, it was dispersed in 100 mL ethanol and 300 mL 2.0 M HCl, and stirred overnight. The red solid was filtered, washed and dried to afford bulk PDIPA. (b) 5.0 mM PDIPA was dispersed in 200 mL deionized water. Add 834 µL of triethylamine (TEA) and stirred for 1 h. Afterwards, add 27.3 mL 4.0 M HCl and then washed and dried to obtain the PDIPA.

### 2.3. Characterization

The morphologies were observed with field emission scanning

electron microscopy (FE-SEM, Hitachi SU-8010), the transmission electron microscope (TEM, Hitachi HT 7700), and the high-resolution transmission electron microscope (HRTEM, JEOL JEM-2100 F). <sup>13</sup>C solid-state nuclear magnetic resonance (<sup>13</sup>C-SSNMR) spectra were acquired with JEOL JNM-ECZ600R. Kelvin probe force microscopy (KPFM, SPM-9700) was utilized to ascertain the surface potential of materials. The UV-vis diffuse reflectance spectroscopy (DRS) were acquired on Agilent Cary 5000 spectrophotometer and Edinburgh F900 fluorescence spectrometer. The Brunauer-Emmet-Teller (BET) specific surface area and pore distribution were recorded with JWGB JW-BK200C. X-ray diffraction (XRD) patterns were measured on Rigaku (Smart-Lab) X-ray diffractometer with Cu K $\alpha$  ( $\lambda = 1.54$  Å). Zeta potential was obtained by Horiba SZ-100. The total organic carbon (TOC) was evaluated on a Jena Multi N/C 2100 TOC/TN. The surface photovoltage (SPV) measurements were conducted with Zolix RAOB05-1, a home-built instrument as previously reported [\[37\]](#). Electron spin resonance (ESR) spectra (JEOL FA-200) was used to identify the main active species.

### 2.4. Photoelectrochemical measurements

Electrochemical workstation (Chenhua CHI660E) was used for the photoelectrochemical measurements. The electrodes employed in this work are as follows: Pt plate as counter electrode, saturated Ag/AgCl as reference electrodes, working electrode as sample coated on indium tin oxide (ITO) glass. 0.1 M aqueous solution of Na<sub>2</sub>SO<sub>4</sub> was used as the electrolyte.

### 2.5. Evaluation of photocatalytic performance

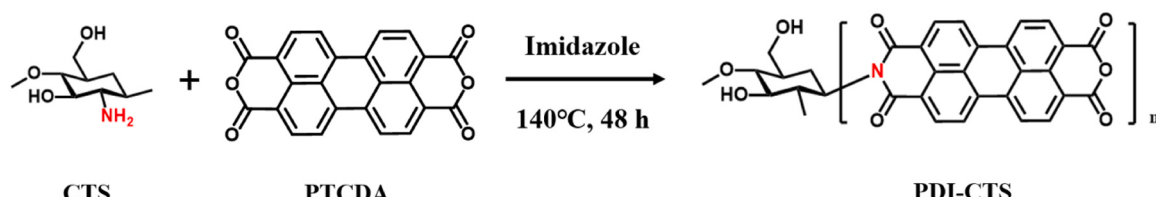
The photocatalytic reaction was conducted in the XPA-7 parallel light reactor. The degradation was conducted in a quartz tube with visible light ( $\lambda \geq 420$  nm). 0.5 mg/mL PDI-CTS was dispersed in deionized water, then added 10 mg/L bisphenol A (BPA) and 1 mmol/L peroxydisulfate (PDS), stirring for 30 min in the dark in advance [\[38\]](#). High performance liquid chromatography (HPLC) was used to detect the real-time content of BPA degradation, and total organic carbon (TOC) analyzer to detect the residual content of degradation products. The degradation rate of the pollutants was evaluated by [Eq. 1](#):

$$r = (c_0 - c)/c_0 \quad (1)$$

$r$  was the degradation rate,  $c_0$  was the initial content of BPA,  $c$  was the detected concentration of BPA in real time.

### 2.6. Theoretical calculation details

Frontier molecular orbital distribution was implemented according to the density functional theory (DFT) via the Gaussian 09 suit of programs (b3lyp, 6-311 G). Surface electrostatic potential (ESP) distribution was calculated and mapped using the Mltiwf program and VMD software.



**Scheme 1.** The synthesis of PDI-CTS.

### 3. Results and discussion

#### 3.1. Construction of the three-dimensional porous PDI-CTS photocatalyst with D-A motif

The PDI-CTS was synthesized by grafting the natural polymer CTS skeleton into PTCDA. The chemical structure and morphology of the synthesized PDI-CTS was first confirmed. The  $^{13}\text{C}$  SSNMR spectrum revealed the chemical environment of C atoms in PDI-CTS (Fig. 1a). The multiple peaks at 120–140 ppm of PDI-CTS and PTCDA were attributed to the conjugated electrons delocalization in the perylene ring. The carbonyl carbon peak of PDI-CTS was blue shifted by 4.8 ppm due to the covalent coupling of CTS to form a new C-N bond [9]. The continuous peaks in the 50–120 ppm range correspond to methylene C of CTS. Combined with the results of Fourier-transformed infrared spectrum (FT-IR) (Fig. S1), the above data showed that PTCDA was successfully covalently linked to CTS. Transmission electron microscopy (TEM) images (Fig. 1b) and scanning electron microscope (SEM) images (Fig. S2) showed that PTCDA exhibited a nanorod-like structure, while PDI-CTS exhibited a large 3D network aggregation structure. Compared to PTCDA, PDI-CTS had almost no crystallization (Fig. S3), while its unique 3D porous structure was expected to achieve higher product adsorption. The isothermal nitrogen adsorption-desorption experiment (Fig. S4) has demonstrated that the 3D network structure of PDI-CTS has the mesopore characteristics. Specifically, the BET specific surface area and pore volume of PDI-CTS are 4.9 and 8.4 times that of PTCDA (Fig. 1c), respectively. This creates more favorable conditions for the adsorption degradation of pollutants. As mentioned above, the 3D porous structure increases the refraction of the light source inside the material, greatly improving the light utilization rate by up to 96.4% (Fig. 1d). Furthermore, the introduction of CTS makes PDI have a more positive potential, which further facilitates the electrostatic adsorption between the material surface and pollutants, promoting degradation and mineralization (Fig. S5).

Furthermore, the intramolecular D-A structure of PDI-CTS was identified. The theoretical calculations of the frontier molecular orbital

distribution showed that the HOMO and LUMO of PDI-CTS are located on the CTS moiety and PDI moiety, respectively (Fig. 1e), which conforms to the characteristics of D-A structure [39]. According to theoretical calculation results, CTS as the electron donors, tends to transfer electrons to PDI. Internal electric field (IEF), which is the local charge distribution in semiconductor materials, is a driving force for photogenerated charge separation and migration [30,40,41]. Independent confirmation has been obtained from Kelvin probe force microscopy (KPFM) measurements. As shown in Fig. 1f, PDI-CTS with D-A structure have a satisfactory surface potential ( $\Delta E=40$  mV), and the black appearing at the edge is the CTS electron aggregation [42]. Under visible light, PDI-CTS showed a significant increase in surface potential ( $\Delta E=66$  mV), confirming that PDI-CTS with D-A structure generates a large amount of photogenerated charge and efficiently separate.

#### 3.2. D-A enhances internal electric field to facilitate charge separation

Generally, the enhancement of the dipole will generate a strong IEF, which can greatly promote photogenerated carrier separation and migration [43–46]. The differences in electronegativity of the modified groups have a significant effect on the electron distributions and molecular dipoles of the PTCDA molecules [47]. As the electrons transferred from CTS to PDI, the molecular dipole of PDI-CTS will increase accordingly. As shown in the electrostatic potential distribution (ESP) (Fig. 2a), PDI-CTS has a larger molecular dipole (3.7428 D) than PTCDA (0.0016 D), thereby creating a robust IEF from PDI to CTS in PDI-CTS. Moreover, the internal electric field could be quantitatively measured by KPFM. As shown in Fig. 2b, the surface potential of PDI-CTS ( $\Delta E=66$  mV) is almost 2.6 times higher than that of PTCDA ( $\Delta E=25$  mV). According to the method proposed by Kanata et al. [48], the magnitude of the internal electric field could be derived from surface charge density and surface voltage, as presented in Fig. S6. The resulting internal electric field magnitude of PDI-CTS is about 6.9 times higher than that of PTCDA (Fig. 2c). Accordingly, the PDI-CTS is characterized with a stronger internal electric field, which would greatly favor charge separation and transportation.

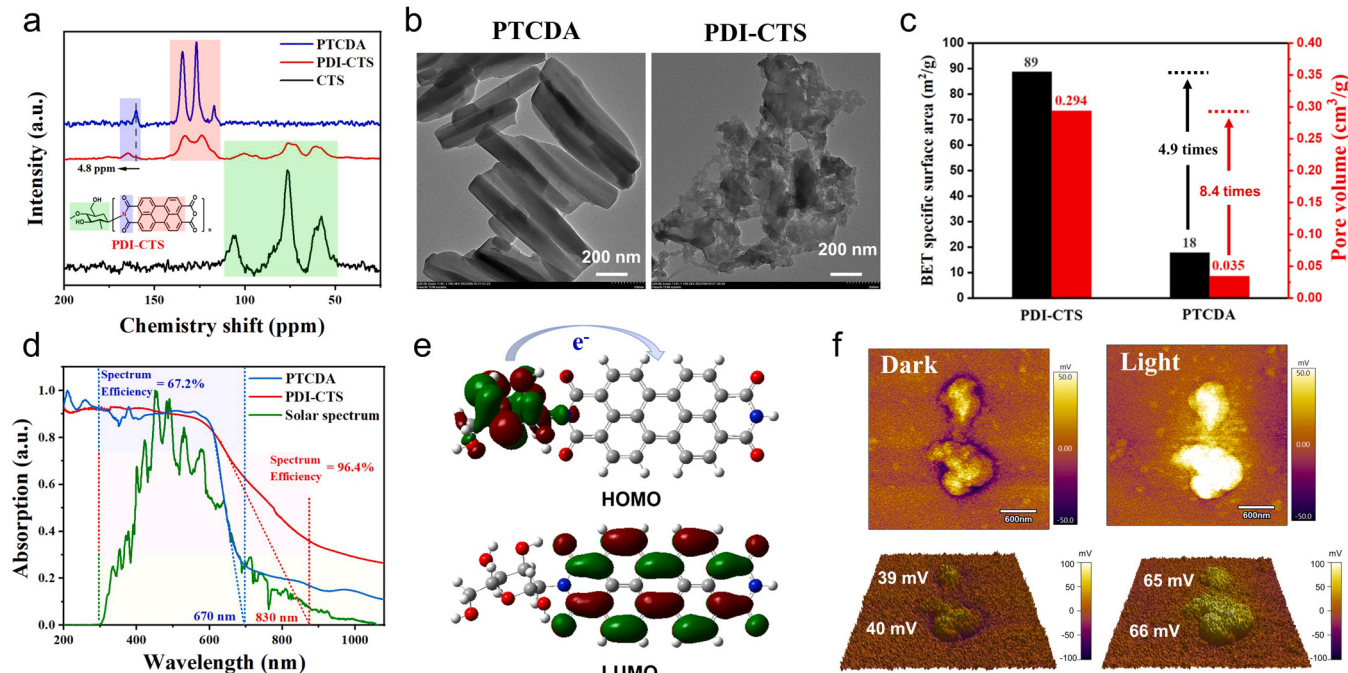


**Fig. 1.** Characterization of 3D porous PDI-CTS with D-A motif. (a)  $^{13}\text{C}$  solid nuclear magnetic spectra of PTCDA, PDI-CTS and CTS. (B) TEM images of PTCDA and PDI-CTS. (c) Comparison of specific surface area and pore volume of PTCDA and PDI-CTS. (d) The UV-vis diffuse reflection spectroscopy of PTCDA, PDI-CTS power and solar spectrum. (e) The frontier molecular orbital distribution of PDI-CTS. (f) The surface potentials measured with KPFM of PDI-CTS before (left) and after (right) visible light radiation.

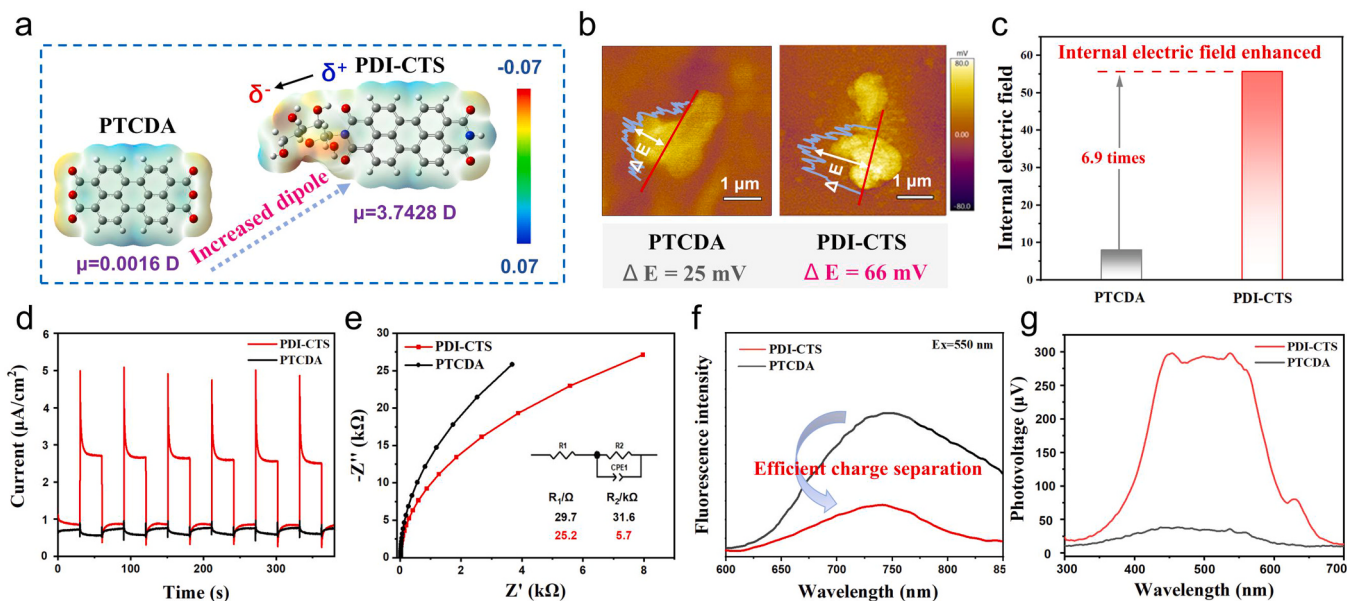


**Fig. 2.** D-A enhances internal electric field of PDI-CTS to promote photogenerated carriers separation. (a) Molecular dipoles and electrons distribution in PTCDA and PDI-CTS, unit of dipole moment: Debye. (b) Surface potential of PTCDA and PDI-CTS detected with KPFM under visible light irradiation. (c) The internal electric field intensity for PTCDA and PDI-CTS. The contrast in PDI-CTS and PTCDA for (d) photocurrent; (e) Electrochemical impedance spectra; (f) Fluorescence emission spectrum; (g) Surface photovoltage.

The charge transfer behavior of the PDI-CTS was evaluated through photoelectron chemical measurement. The photocurrent of PDI-CTS is as high as  $2.93 \mu\text{A}/\text{cm}^2$  compared to PTCDA (Fig. 2d), further indicating

the excellent separation of carriers in PDI-CTS driven by the internal electric field. The arc radius of electrochemical impedance spectroscopy (EIS) can be used to judge the resistance of charge transfer. PDI-CTS

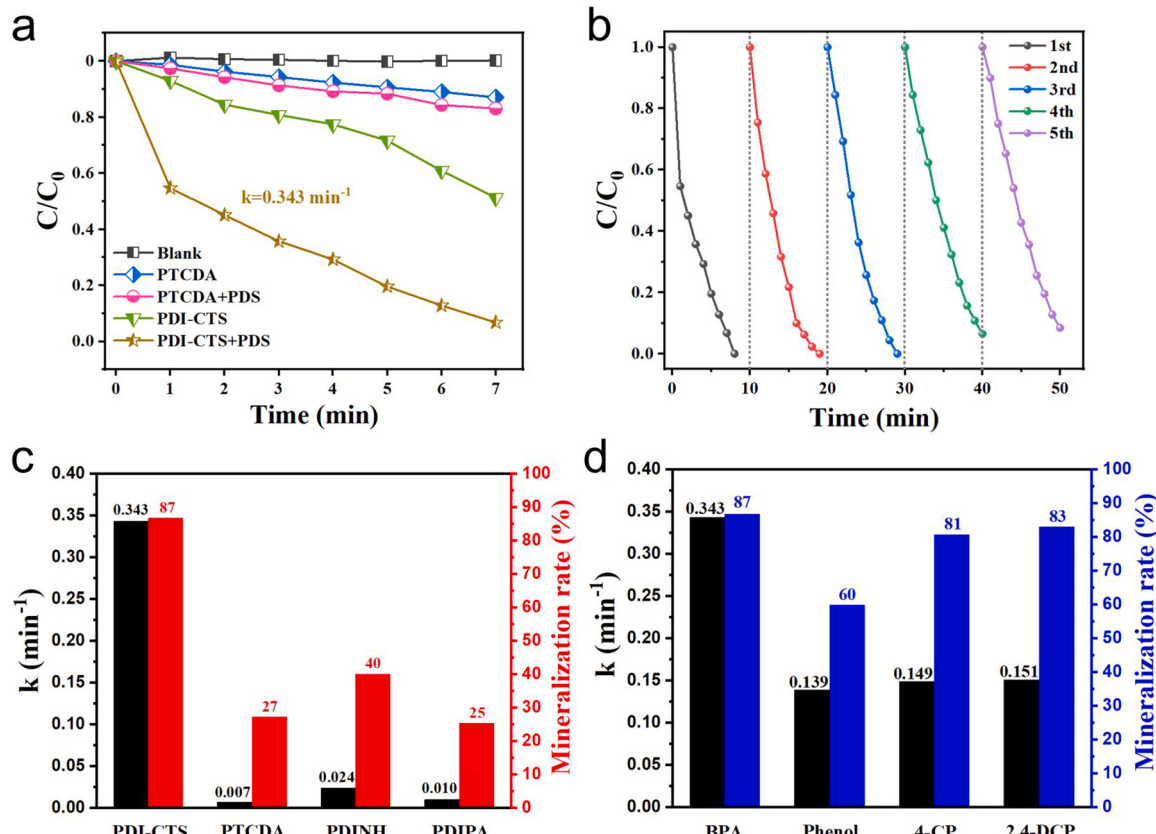


**Fig. 3.** The degradation performance of PDI-CTS by PDS activation. (a) The degradation rate of BPA by PTCDA and PDI-CTS with or without PDS (1 mM) activation in visible light. In the degradation experiment, the BPA concentration was  $10 \text{ mg/L}$  and the PDI-CTS concentration was  $0.5 \text{ mg/mL}$ , respectively. (b) The cyclic degradation of BPA by PDI-CTS with PDS activation. The apparent rate constant (left) and mineralization rate (right) of (c) BPA degradation using different PDI-based photocatalysts with PDS activation, as well as (d) different organic pollutants degradation by PDI-CTS with PDS activation.

exhibited a smaller arc radius compared with PTCDA, and  $R_2$  (the fitted charge transfer resistance) was only  $5.7\text{ k}\Omega$  (Fig. 2e), indicating the faster charge transfer kinetics of PDI-CTS. Besides, fluorescence intensity can reflect the efficiency of charge separation, as the fluorescence emission is induced by recombination of photogenerated  $\text{h}^+$  and  $\text{e}^-$  pairs. As shown in Fig. 2f, the obvious fluorescence emission attenuation of PDI-CTS than PTCDA proves that the internal electric field facilitates photoinduced electron transfer. Surface photogenerated voltage (SPV) spectra [49] can also use to verify the charge transfer, which is formed when  $\text{h}^+$  and  $\text{e}^-$  are separated by a built-in electric field and diffused into the near-surface space charge region (SCR) of the semiconductor driven by a concentration gradient. PDI-CTS shows a strong positive SPV response at 400–600 nm (Fig. 2g), which is 10.4 folds higher than those of PTCDA, indicating that the extraordinary charge separation efficiency of PDI-CTS. The above results show that the efficient migration of  $\text{h}^+$  and  $\text{e}^-$  is facilitated by the strong built-in electric field established from PDI to CTS. Furthermore, the changes of energy band structure are further revealed in Fig. S7.

### 3.3. High photocatalytic degradation enhanced by PDS activation

As a toxic organic pollutant, Bisphenol A (BPA) was selected to evaluate the degradation performance of PDI-CTS. Under visible light, PDS could not achieve the degradation due to its relatively stability. As shown in Fig. 3a, PTCDA had little changes in degradation, while PDI-CTS had a relatively good degradation effect on BPA due to its

excellent charge separation efficiency as well as the superior pollutant adsorption (Fig. S8). Interestingly, the introduction of PDS significantly improved the degradation activities of both PTCDA and PDI-CTS. It is worth noting that the PDI-CTS+PDS system can completely degrade BPA within 7 min, with the rate constant as high as  $0.343\text{ min}^{-1}$ , indicating that PDI-CTS has excellent performance in activating PDS to efficiently degrade pollutants. Furthermore, PDI-CTS maintained high activity over five cycles of photocatalytic degradation (Fig. 3b). The covalent bonding of PDI to the polymer skeleton of CTS ensured the reusability of PDI-CTS, as evidenced by its unchanged SEM morphology and FT-IR spectrum before and after the degradation cycle (Fig. S9). Under the simulated sunlight (AM 1.5 G), the degradation rate of BPA was slightly higher than under visible light (Fig. S10), demonstrating the full spectral response and high light utilization of PDI-CTS.

Compared to other common PDI-based photocatalysts (PTCDA, PDINH, PDIPA), PDI-CTS exhibits superior photocatalytic performance after activating PDS (Fig. S11). The unique 3D porous structure of PDI-CTS provides abundant active sites for BPA adsorption and PDS activation, while  $\text{PDI}^\cdot$  produced by D-A electron transfer further promotes rapid activation of PDS for efficient BPA degradation. Specifically, the degradation rate constant of PDI-CTS is 14.2 times higher than that of PDINH with better performance (Fig. 3c). Notably, the mineralization rate of BPA reached 87%, which was at least 47% higher than that of other materials. In addition, the degradation activity of PDI-CTS+PDS for phenol, *p*-chlorophenol (4-CP) and 2,4-dichlorophenol (2,4-DCP) was further evaluated (Fig. S12). The results showed that the

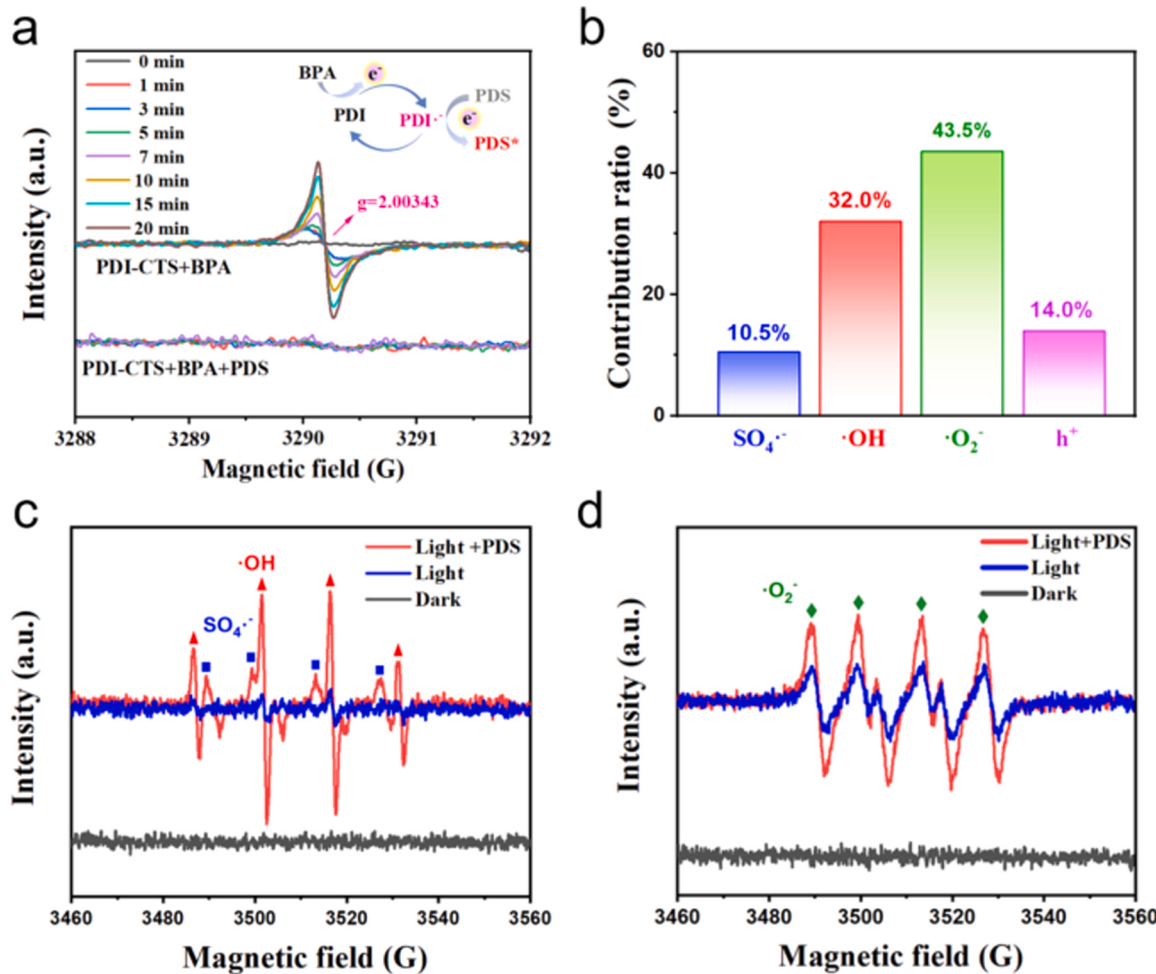


**Fig. 4.** PDS activation and synergistic advanced oxidation of multiple reactive species. (a) ESR spectra of PDI-CTS+BPA before and after introduction of PDS. (b) The relative contribution ratio of different active species in BPA degradation by PDI-CTS. (c) ESR spectra of  $\cdot\text{OH}$  (red diamond) and  $\text{SO}_4^{\cdot-}$  (blue diamond) in PDI-CTS. (d) ESR spectra of  $\cdot\text{O}_2^{\cdot-}$  in PDI-CTS.

degradation rate constant of PDI-CTS+PDS for these organic pollutants was above  $0.1 \text{ min}^{-1}$ , with impressive mineralization rates of 60% for phenol, 81% for 4-CP, and 83% for 2,4-DCP, respectively (Fig. 3d). These above results demonstrate that PDI-CTS can rapidly activate PDS to achieve efficient degradation as well as deep mineralization of various organic pollutants, making it a highly active and universal materials with great potential for visible light-driven wastewater purification application.

### 3.4. D-A facilitated PDS activation in efficient degradation

Furthermore, the PDS activated-mechanism by PDI-CTS was studied. In the electron spin resonance (ESR) spectra (Fig. 4a), no signal was observed in PDI-CTS+BPA system in the dark. However, PDI<sup>·-</sup> signal enhanced after 1 min of illumination, and time-dependent signal ( $g=2.00343$ ) enhancement was shown within 20 min, indicating that electrons were stored in the form of PDI<sup>·-</sup> [50,51]. Upon the introduction of PDS, PDI<sup>·-</sup> signal was drastically quenched, suggesting that PDS can rapidly consume the electrons of PDI<sup>·-</sup> and converted it back to PDI. Driven by visible light, the transfer of electrons from CTS to PDI will lead to the formation of more PDI<sup>·-</sup>. Consequently, PDS can quickly capture the accumulated electrons, resulting in a large number of holes accumulating on the surface of the material.

To further clarify the PDS activated-mechanism by PDI-CTS, the main active species were identified in the degradation. Using BPA as the target pollutant, it is proved that these active species can reduce the photocatalytic degradation rate in different degrees (Fig. S13). As shown in Fig. 4b, the relative contribution rates of these active species were calculated as follows: SO<sub>4</sub><sup>·-</sup> was 10.5%, ·O<sub>2</sub> was 32.0%, ·OH was 43.5%, and h<sup>+</sup> was 14.0%, respectively. To sum up, ·O<sub>2</sub> was the primary active species to promote degradation, and the contribution rates of SO<sub>4</sub><sup>·-</sup> and ·OH produced by PDS activation were almost equivalent to ·O<sub>2</sub>.

Next, the above free radicals were detected with ESR. Fig. 4c displays the ESR signals of ·OH (red diamond) and SO<sub>4</sub><sup>·-</sup> (blue diamond). A weak ·OH signal appeared after irradiation for 5 min, attributed to the loss electrons from the hydroxyl group on BPA. When adding of PDS, a significant SO<sub>4</sub><sup>·-</sup> signal appears after irradiation due to the activation of PDS. Subsequently, SO<sub>4</sub><sup>·-</sup> rapidly oxidize H<sub>2</sub>O, resulting in a substantial enhancement of the ·OH signal. In Fig. 4d, no ·O<sub>2</sub> signal was observed in the PDI-CTS system at dark, while O<sub>2</sub> signal appears after illumination due to the interaction between e<sup>-</sup> and O<sub>2</sub>. Similarly, ·O<sub>2</sub> signal was enhanced significantly after the addition of PDS and illumination, indicating that PDS activation could promote more ·O<sub>2</sub> produced [52]. Notably, ·O<sub>2</sub> had a very high degradation contribution rate, suggesting that the enriched electrons generated by the D-A structure could also promote the reduction of O<sub>2</sub>, thus greatly accelerating the degradation process.

As shown in Fig. 5, the mechanism of PDI-CTS activated PDS for

efficient photocatalytic advanced oxidation was proposed. Under visible light, the unique D-A structure created an internal electric field that promotes the separation of e<sup>-</sup> and h<sup>+</sup>. In the conduction band, e<sup>-</sup> reacts with PDI so as to form PDI<sup>·-</sup>, which can react with O<sub>2</sub> to form ·O<sub>2</sub> and can also generate plenty of ·OH and SO<sub>4</sub><sup>·-</sup> through the rapid PDS activation. The synergistic oxidation of these radicals greatly improves the degradation rate. Moreover, 3D porous PDI-CTS exhibited superior pollutant adsorption capabilities, and the trapping of electrons on PDI<sup>·-</sup> by PDS greatly promotes the migration of h<sup>+</sup> towards the valence band, which is of great benefit to the deep mineralization of strongly oxidized pollutants.

### 4. Conclusions

In summary, three-dimensional porous PDI-CTS was successfully fabricated through covalent bonding. The donor-acceptor (D-A) interaction in PDI-CTS induced a large dipole moment and formed a robust built-in electric field, facilitating the separation and transport of photogenerated carriers. Under visible light, PDI-CTS efficiently activate PDS, leading to the degradation of various organic pollutants with a high mineralization rate. The multiple active sites in PDI-CTS enhanced the adsorption with pollutants and PDS, while the PDI<sup>·-</sup> rapidly activated PDS, generating a variety of free radicals and accelerating the degradation of BPA. Moreover, photocatalytic-assisted PDS activation further promoted the migration of strongly oxidized h<sup>+</sup> to the surface of PDI-CTS, contributing to the deep mineralization of organic pollutants. This work provides a photocatalytic advanced oxidation strategy for promoting photogenerated charge carriers through D-A interaction, which has great application potential for the efficient degradation and deep mineralization of environmental wastewater.

### CRediT authorship contribution statement

**Huang Sijie:** Methodology, Data curation, Writing – original draft. **Zhang Hanjie:** Conceptualization, Visualization. **Li Wenting:** Investigation, Formal analysis, Visualization, Writing – review & editing, Project administration. **Liu Liping:** Resources, Project administration, Writing – review & editing. **Xu Jingyi:** Visualization, Project administration. **Chong Meichi:** Methodology, Investigation. **Li Junshan:** Project administration. **Zhu Yongfa:** Resources, Project administration, Supervision, Funding acquisition.

### Declaration of Competing Interest

The authors declare that they have no known competing financial interests or personal relationships that could have appeared to influence the work reported in this paper.

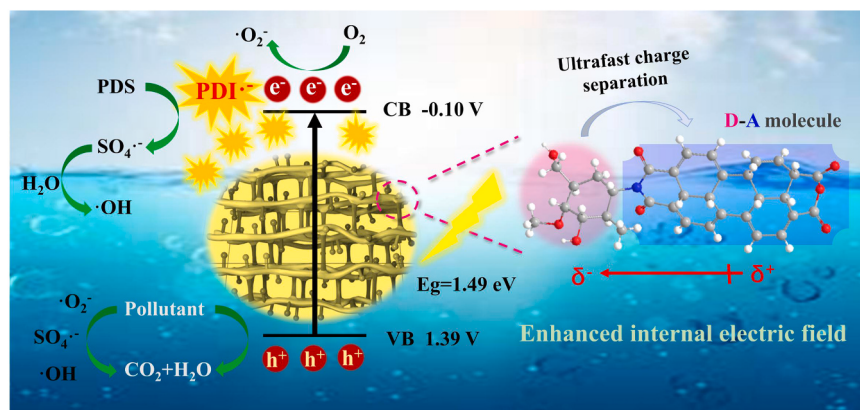


Fig. 5. Mechanism diagram of 3D porous PDI-CTS photocatalyst with D-A characteristics activating PDS to degrade pollutants under visible light.

## Data Availability

Data will be made available on request.

## Acknowledgements

The authors acknowledge financial support from the National Natural Science Foundation of China (22136002), National Key Research and Development Project of China (2020YFA0710304), Special Fund Project of Jiangsu Province for Scientific and Technological Innovation in Carbon Peaking and Carbon Neutrality (BK20220023).

## Appendix A. Supporting information

Supplementary data associated with this article can be found in the online version at [doi:10.1016/j.apcatb.2024.123790](https://doi.org/10.1016/j.apcatb.2024.123790).

## References

- [1] Y. Zhang, J.B. Zhou, X. Chen, L. Wang, W.Q. Cai, Coupling of heterogeneous advanced oxidation processes and photocatalysis in efficient degradation of tetracycline hydrochloride by Fe-based MOFs: Synergistic effect and degradation pathway, *Chem. Eng. J.* 369 (2019) 745–757.
- [2] S.D. Yan, Y. Shi, Y.F. Tao, H. Zhang, Enhanced persulfate-mediated photocatalytic oxidation of bisphenol A using bioelectricity and a g-C<sub>3</sub>N<sub>4</sub>/Fe<sub>2</sub>O<sub>3</sub> heterojunction, *Chem. Eng. J.* 359 (2019) 933–943.
- [3] Y.B. Wang, X. Zhao, D. Cao, Y. Wang, Y.F. Zhu, Peroxymonosulfate enhanced visible light photocatalytic degradation bisphenol A by single-atom dispersed Ag mesoporous g-C<sub>3</sub>N<sub>4</sub> hybrid, *Appl. Catal. B: Environ.* 211 (2017) 79–88.
- [4] F. Ghanbari, M. Moradi, Application of peroxymonosulfate and its activation methods for degradation of environmental organic pollutants: review, *Chem. Eng. J.* 310 (2017) 41–62.
- [5] B.T. Zhang, Y. Zhang, Y.H. Teng, M.H. Fan, Sulfate radical and its application in decontamination technologies, *Crit. Rev. Environ. Sci. Tec.* 45 (2015) 1756–1800.
- [6] P. Devi, U. Das, A.K. Dalai, chemical oxidation: Principle and applications of peroxide and persulfate treatments in wastewater systems, *Sci. Total Environ.* 571 (2016) 643–657.
- [7] M.M. Ahmed, S. Barbat, P. Doumenq, S. Chiron, Sulfate radical anion oxidation of diclofenac and sulfamethoxazole for water decontamination, *Chem. Eng. J.* 197 (2012) 440–447.
- [8] A.D. Bokare, W. Choi, Review of iron-free Fenton-like systems for activating H<sub>2</sub>O<sub>2</sub> in advanced oxidation processes, *J. Hazard. Mater.* 275 (2014) 121–135.
- [9] W.T. Li, H.J. Zhang, S.J. Huang, J.Y. Xu, L.P. Liu, J.S. Li, J.F. Jing, Y.F. Zhu, Electron-enriched supramolecular PDI-SiO<sub>2</sub> promoting PDS activation for enhanced photocatalytic advanced oxidation, *Appl. Catal. B: Environ.* 340 (2024) 123262.
- [10] J.G. Yu, J. Jin, B. Cheng, M. Jaroniec, A noble metal-free reduced graphene oxide-CdS nanorod composite for the enhanced visible-light photocatalytic reduction of CO<sub>2</sub> to solar fuel, *J. Mater. Chem. A* 2 (2014) 3407–3416.
- [11] Z.Q. He, Y.Q. Shi, C. Gao, L.N. Wen, J.M. Chen, S. Song, BiOCl/BiVO<sub>4</sub> p-n heterojunction with enhanced photocatalytic activity under visible-light irradiation, *J. Phys. Chem. C.* 118 (2014) 389–398.
- [12] H.F. Lin, L.P. Li, M.L. Zhao, X.S. Huang, X.M. Chen, G.S. Li, R.C. Yu, Synthesis of high-quality brookite TiO<sub>2</sub> single-crystalline nanosheets with specific facets exposed: tuning catalysts from inert to highly reactive, *J. Am. Chem. Soc.* 134 (2012) 8328–8331.
- [13] K. Vinodgopal, P.V. Kamat, Enhanced rates of photocatalytic degradation of an azo-dye using SnO<sub>2</sub>/TiO<sub>2</sub> coupled semiconductor thin-films, *Environ. Sci. Technol.* 29 (1995) 841–845.
- [14] Z.J. Zhang, X.J. Chen, H.J. Zhang, W.X. Liu, W. Zhu, Y.F. Zhu, A highly crystalline perylene imidepolymer with the robust built-in electric field for efficient photocatalytic water oxidation, *Adv. Mater.* 32 (2020) 1907746.
- [15] T.A. Shifa, F.M. Wang, Z.Z. Cheng, P. He, Y. Liu, C. Jiang, Z.X. Wang, J. He, High crystal quality 2D manganese phosphorus trichalcogenide nanosheets and their photocatalytic activity, *Adv. Funct. Mater.* 28 (2018) 1800548.
- [16] S.N. Basahel, T.T. Ali, M. Mokhtar, K. Narasimharao, Influence of crystal structure of nanosized ZrO<sub>2</sub> on photocatalytic degradation of methyl orange, *Nanoscale Res. Lett.* 10 (2015) 73.
- [17] X.J. Chen, Q. Chen, W.J. Jiang, Z. Wei, Y.F. Zhu, Separation-free TiO<sub>2</sub>-graphene hydrogel with 3D network structure for efficient photoelectrocatalytic mineralization, *Appl. Catal. B: Environ.* 211 (2017) 106–113.
- [18] M. Zhang, W.J. Luo, Z. Wei, W.J. Jiang, D. Liu, Y.F. Zhu, Separation free C<sub>3</sub>N<sub>4</sub>/SiO<sub>2</sub> hybrid hydrogels as high active photocatalysts for TOC removal, *Appl. Catal. B: Environ.* 194 (2016) 105–110.
- [19] W.J. Jiang, W.J. Luo, R.L. Zong, W.Q. Yao, Z.P. Li, Y.F. Zhu, Polyaniline/carbon nitride nanosheets composite hydrogel: a separation-free and high-efficient photocatalyst with 3D hierarchical structure, *Small* 12 (2016) 4370–4378.
- [20] W.J. Jiang, Y.F. Liu, J. Wang, M. Zhang, W.J. Luo, Y.F. Zhu, Separation-free polyaniline/TiO<sub>2</sub> 3D hydrogel with high photocatalytic activity, *Adv. Mater. Interfaces* 3 (2016) 1500502.
- [21] J.J. Yang, D.M. Chen, Y. Zhu, Y.M. Zhang, Y.F. Zhu, <sup>3</sup>D-<sup>3</sup>D porous Bi<sub>2</sub>WO<sub>6</sub>/graphene hydrogel composite with excellent synergistic effect of adsorption-enrichment and photocatalytic degradation, *Appl. Catal. B: Environ.* 205 (2017) 228–237.
- [22] M. Zhang, W.J. Jiang, D. Liu, J. Wang, Y.F. Liu, Y.Y. Zhu, Y.F. Zhu, Photodegradation of phenol via C<sub>3</sub>N<sub>4</sub>-agar hybrid hydrogel 3D photocatalysts with free separation, *Appl. Catal. B: Environ.* 183 (2016) 263–268.
- [23] J. Yang, H. Miao, Y.X. Wei, W.L. Li, Y.F. Zhu,  $\pi$ - $\pi$  Interaction between self-assembled perylene diimide and 3D graphene for excellent visible-light photocatalytic activity, *Appl. Catal. B: Environ.* 240 (2019) 225–233.
- [24] W.J. Jiang, Y.F. Zhu, G.X. Zhu, Z.J. Zhang, X.J. Chen, W.Q. Yao, Three-dimensional photocatalysts with a network structure, *J. Mater. Chem. A* 5 (2017) 5661–5679.
- [25] Y. Guo, W.X. Shi, Y.F. Zhu, Internal electric field engineering for steering photogenerated charge separation and enhancing photoactivity, *Ecomat* 1 (2019) e12007.
- [26] Y. Su, L. Zhang, W.Z. Wang, D.K. Shao, Internal electric field assisted photocatalytic generation of hydrogen peroxide over BiOCl with HCOOH, *ACS Sustain. Chem. Eng.* 6 (2018) 8704–8710.
- [27] M. Li, H.W. Huang, S.X. Yu, N. Tian, Y.H. Zhang, Facet, junction and electric field engineering of bismuth-based materials for photocatalysis, *Chemcatchem* 10 (2018) 4477–4496.
- [28] Y. Chen, W.Y. Yang, S. Gao, L.G. Zhu, C.X. Sun, Q. Li, Internal polarization modulation in Bi<sub>2</sub>MoO<sub>6</sub> for photocatalytic performance enhancement under visible-light illumination, *Chemsuschem* 11 (2018) 1521–1532.
- [29] J. Li, G.M. Zhan, Y. Yu, L.Z. Zhang, Superior visible light hydrogen evolution of Janus bilayer junctions via atomic-level charge flow steering, *Nat. Commun.* 7 (2016) 11480.
- [30] J. Li, L.J. Cai, J. Shang, Y. Yu, L.Z. Zhang, Giant enhancement of internal electric field boosting bulk charge separation for photocatalysis, *Adv. Mater.* 28 (2016) 4059–4064.
- [31] J. Li, L.Z. Zhang, Y.J. Li, Y. Yu, Synthesis and internal electric field dependent photoreactivity of Bi<sub>3</sub>O<sub>4</sub>Cl single-crystalline nanosheets with high {001} facet exposure percentages, *Nanoscale* 6 (2014) 167–171.
- [32] J. Li, Y. Yu, L.Z. Zhang, Bismuth oxyhalide nanomaterials: layered structures meet photocatalysis, *Nanoscale* 6 (2014) 8473–8488.
- [33] Z.J. Zhang, Y.F. Zhu, X.J. Chen, H.J. Zhang, J. Wang, A full-spectrum metal-free porphyrin supramolecular photocatalyst for dual functions of highly efficient hydrogen and oxygen evolution, *Adv. Mater.* 31 (2019) e1806626.
- [34] A.S. Weigarten, A.J. Dannenhoffer, R.V. Kazantsev, H. Sai, D.X. Huang, S.I. Stupp, Chromophore dipole directs morphology and photocatalytic hydrogen generation, *J. Am. Chem. Soc.* 140 (2018) 4965–4968.
- [35] H.V. Lutze, S. Bircher, I. Rapp, N. Kerlin, R. Bakour, M. Geisler, C. von Sonntag, T. C. Schmidt, Degradation of chlorotriazine pesticides by sulfate radicals and the influence of organic matter, *Environ. Sci. Technol.* 49 (2015) 1673–1680.
- [36] W.D. Oh, Z.L. Dong, T.T. Lim, Generation of sulfate radical through heterogeneous catalysis for organic contaminants removal: current development, challenges and prospects, *Appl. Catal. B: Environ.* 194 (2016) 169–201.
- [37] J.F. Jing, J. Yang, W.L. Li, Z.H. Wu, Y.F. Zhu, Construction of interfacial electric field via dual-porphyrin heterostructure boosting photocatalytic hydrogen evolution, *Adv. Mater.* 34 (2022) 2106807.
- [38] S. Waclawek, H.V. Lutze, K. Grüber, V.V.T. Padil, M. Cerník, D.D. Dionysiou, Chemistry of persulfates in water and wastewater treatment: a review, *Chem. Eng. J.* 330 (2017) 44–62.
- [39] W.Q. Wei, D. Liu, Z. Wei, Y.F. Zhu, Short-range  $\pi$ - $\pi$  stacking assembly on P25 TiO<sub>2</sub> nanoparticles for enhanced visible-light photocatalysis, *ACS Catal.* 7 (2017) 652–663.
- [40] Y. Zheng, T.F. Zhou, X.D. Zhao, W.K. Pang, H. Gao, S. Li, Z. Zhou, H.K. Liu, Z. P. Guo, Atomic interface engineering and electric-field effect in ultrathin Bi<sub>2</sub>MoO<sub>6</sub> nanosheets for superior lithium ion storage, *Adv. Mater.* 29 (2017) 1700396.
- [41] M.A. Fox, E. Galloppini, Electric field effects on electron transfer rates in dichromophoric peptides: the effect of helix unfolding, *J. Am. Chem. Soc.* 119 (1997) 5277–5285.
- [42] X.J. Chen, Y. Xu, X.G. Ma, Y.F. Zhu, Large dipole moment induced efficient bismuth chromate photocatalysts for wide-spectrum driven water oxidation and complete mineralization of pollutants, *Natl. Sci. Rev.* 7 (2020) 652–659.
- [43] L.P. Liu, H.B. Meng, Y.Q. Chai, X.J. Chen, J.Y. Xu, X.L. Liu, W.X. Liu, D.M. Guldi, Y. F. Zhu, Enhancing built-in electric fields for efficient photocatalytic hydrogen evolution by encapsulating C<sub>60</sub> fullerene into zirconium-based metal-organic frameworks, *Angew. Chem. Int. Ed.* 62 (2023) e202217897.
- [44] Z.Z. Yu, K. Yang, C.L. Yu, K.Q. Lu, W.Y. Huang, L. Xu, L.X. Zou, S.B. Wang, Z. Chen, J. Hu, Y. Hou, Y.F. Zhu, Steering unit cell dipole and internal electric field by highly dispersed Er atoms embedded into NiO for Efficient CO<sub>2</sub> photoreduction, *Adv. Funct. Mater.* 32 (2022) 2111999.
- [45] J. Yang, J.F. Jing, Y.F. Zhu, A full-spectrum porphyrin-fullerene D-A supramolecular photocatalyst with giant built-in electric field for efficient hydrogen production, *Adv. Mater.* 33 (2021) 2101026.
- [46] F. Chen, H.W. Huang, L. Guo, Y.H. Zhang, T.Y. Ma, The role of polarization in photocatalysis, *Angew. Chem. Int. Ed.* 58 (2019) 10061–10073.
- [47] J. Wang, W. Shi, D. Liu, Z.J. Zhang, Y.F. Zhu, D. Wang, Supramolecular organic nanofibers with highly efficient and stable visible light photooxidation performance, *Appl. Catal. B: Environ.* 202 (2017) 289–297.
- [48] T. Kanata-Kito, M. Matsunaga, H. Takakura, Y. Hamakawa, T. Nishino, F.H. Pollak, M. Cardona, D.E. Aspnes, Photoreflectance characterization of built-in potential in MBE-produced as-grown GaAs surface, *Proc. SPIE* 1286 (1990) 56–65.

[49] R.T. Chen, F.T. Fan, T. Dittrich, C. Li, Imaging photogenerated charge carriers on surfaces and interfaces of photocatalysts with surface photovoltage microscopy, *Chem. Soc. Rev.* 47 (2018) 8238–8262.

[50] X. Yang, Y. Li, G.Y. Chen, H.R. Liu, L. Li Yuan, L. Yang, D. Liu, ZnSnO<sub>3</sub> quantum dot/perylene diimide supramolecular nanorod heterojunction photocatalyst for efficient phenol degradation, *ACS Appl. Nano Mater.* 5 (2022) 9829–9839.

[51] I. Ghosh, T. Ghosh, J.I. Bardagi, B. König, Reduction of aryl halides by consecutive visible light-induced electron transfer processes, *Science* 346 (2014) 725–728.

[52] Q.Y. Ji, X.Y. Cheng, Y.J. Wu, W.M. Xiang, H. He, Z. Xu, C.M. Xu, C.D. Qi, S.Y. Li, L.M. Zhang, S.G. Yang, Visible light absorption by perylene diimide for synergistic persulfate activation towards efficient photodegradation of bisphenol A, *Appl. Catal. B: Environ.* 282 (2021) 119579.